van der Waals Ferroelectric Halide Perovskite Artificial Synapse

Yao Cai, Yang Hu, Zhizhong Chen, Jie Jiang, Lifu Zhang, Yuwei Guo, Saloni Pendse, Ru Jia, Jiahe Zhang, Xiaolong Ma, Chengliang Sun, and Jian Shi

Phys. Rev. Applied **18**, 014014 — Published 7 July 2022

DOI: 10.1103/PhysRevApplied.18.014014

Van der Waals ferroelectric halide perovskite artificial synapse

Yao Cai[1,2,†], Yang Hu[2,†], Zhizhong Chen[2], Jie Jiang[2], Lifu Zhang[2], Yuwei Guo[2], Saloni Pendse[2], Ru Jia[2], Jiahe Zhang[3], Xiaolong Ma[3], Chengliang Sun[1,*], Jian Shi[2,4,*]

†These authors contributed equally to this work.

[1] The Institute of Technological Sciences, Wuhan University, Wuhan 430072, China
[2] Department of Materials Science and Engineering, Rensselaer Polytechnic Institute, Troy, NY 12180, USA
[3] Hongyi Honor College of Wuhan University, Wuhan 430072, China
[4] Center for Materials, Devices, and Integrated Systems, Rensselaer Polytechnic Institute, Troy, NY 12180, USA

Keywords: van der Waals perovskite, domain switching, synaptic operation, neuromorphic computing

Abstract

Ferroelectricity has been shown promising in emulating the synaptic characteristics of human brains. Utilizing ferroelectricity for brain-inspired computing has been proposed as a feasible route in addressing technical challenges in memory and computing. In this work, we demonstrate the use of ferroelectric van der Waals (vdW) halide perovskite for synaptic emulation. The two-terminal ferroelectric synapse based a vdW material (R)-(−)-1-cyclohexylethylammonium)PbI_3 (R-CYHEAPbI_3) exhibits voltage pulse-dependent weights modulation with a total on/off ratio of 50 and good endurance up to 10^7 cycles. The energy consumptions per synaptic operation for both short-term plasticity and long-term plasticity reach pico joule level. The device also shows reasonable write linearity and small cycle-to-cycle variation, as well as promising spike timing dependent plasticity and paired-pulse facilitation function. Numerical simulations with R-CYHEAPbI_3 synapses-based neural network suggest the potential of R-CYHEAPbI_3 synapses for pattern recognition. Ferroelectric vdW halide perovskites would render opportunities in exploiting their dimensionality, superior optoelectronic properties, and their mild materials processing condition for engineering the synaptic device performance.

Main text

I. INTRODUCTION

Artificial synapses, as one of essential building blocks in the neuromorphic circuits, mimic the way biological synapses memorize and learn in human brain.[1-6] In neuromorphic circuits, learning is achieved by the tuning of the weight of each synaptic device following certain mathematical algorithms.[1] To realize efficient parallel learning and inference in neuromorphic computing, synaptic devices must carry attributes of linear and symmetric weight-excitation relation, a large number of non-volatile states and fast switching speed.[1, 7, 8]

Among extensive demonstrations of synaptic devices,[9-11] ferroelectricity-enabled multi-state memristive synapse has recently attracted some attentions.[11-15] In a ferroelectric synapse, non-volatile synaptic weights are encoded in ferroelectric polarization. The multilevel polarization states of ferroelectrics are mainly due to the multiple-domain structure. So far the mostly studied ferroelectric materials for synapse have been mainly focused on oxide ferroelectrics. They show a large polarization, reasonable number of synaptic states, good endurance and retention. However, materials processability and defects (e.g. vacancies) have been issues for their scalability and reliable operation.[16] Expanding the materials space beyond oxides for synaptic application may provide new opportunities for addressing some issues that oxides ferroelectrics suffer from. Van der Waals (vdW) halide perovskites have exhibited superior electrical and optical properties with great feasibility in materials processing and device miniaturization.[17-21] The demonstration of ferroelectric synapse in halide perovskite would provide us a new material platform in designing synapses with demanded characteristics.[20, 22-25]

Herein, we demonstrate the use of an one-dimensional (1D) vdW halide perovskite ((R)-(−)-1-cyclohexylethylammonium)PbI_3 (R-CYHEAPbI_3) for ferroelectric synapses. As shown in Fig. 1(a), in our ferroelectric R-CYHEAPbI_3, Pb-I atoms crystallize to 1D face-sharing octahedral chains loosely bound by organic ligands. The inorganic lead iodine octahedra dominate semiconducting properties, while organic molecules are responsible for switchable ferroelectric polarization.[26] The vdW nature of this material allows the structural flexibility in enabling both band transport (PbI_6) and ferroelectricity (organic groups). We have successfully achieved the synaptic plasticity in R-CYHEAPbI_3 ferroelectric diode, which is featured by a reasonable number of non-volatile states, pulse-dependent weight update, good endurance, nearly linear weight-updates, small cycle-cycle variances and nondestructive read operations. Based on such device, we further demonstrated short- and long-term plasticity (STP and LTP), spike timing dependent plasticity (STDP) and paired-pulse facilitation (PPF) function. With the experimental synaptic characteristics, a parallel training with back propagation algorithm is executed in a crossbar-based two-layer neural network with which a high classification accuracy has been achieved.

II. METHODS AND CHARACTERIZATION

Figure 1(b) and 1(c) show the atomic crystal structures of R-CYHEAPbI_3. R-CYHEAPbI_3 belongs to $P2_1$space group and has lattice constants a = 8.628 Å, b = 8.211 Å, c = 22.994 Å and β = 89.5121° at room temperature.[26, 27] Compared with most conventional ferroelectrics of $BaTiO_3$ and $Pb(Zr_xTi_{1-x})O_3$,[28] the halide perovskite R-CYHEAPbI_3 are featured by large lattice constants and low processing temperature due to the existence of large organic groups and vdW gaps (Fig. 1(a)). We employ a solution method to synthesize R-CYHEAPbI_3 mm-sized bulk crystals and apply a standard spin-coating approach to synthesize thin film form (see Experimental Section in Supplemental Material[29]). For the spin coating method, briefly, the saturated solution of R-CYHEAPbI_3 was spin-coated on the substates and then film is crystallized. Figure 1(d) shows the x-ray diffraction (XRD) patterns of both R-CYHEAPbI_3 powders (grinded from their single crystals) and spin-coated film on silicon substrate with Au electrode deposited. With the simulated XRD result of ideal R-CYHEAPbI_3 crystal from our previous research,[26] we can confirm the synthesis and deposition of expected polar $P2_1$ phase (Experimental Section in Supplemental Material). In the spin-coated film with Au electrode, XRD result shows the presence of Au (111) peak. The simple spin-coating approach in fabricating the R-CYHEAPbI_3 thin film makes it easily be integrated on many technological important substrates.

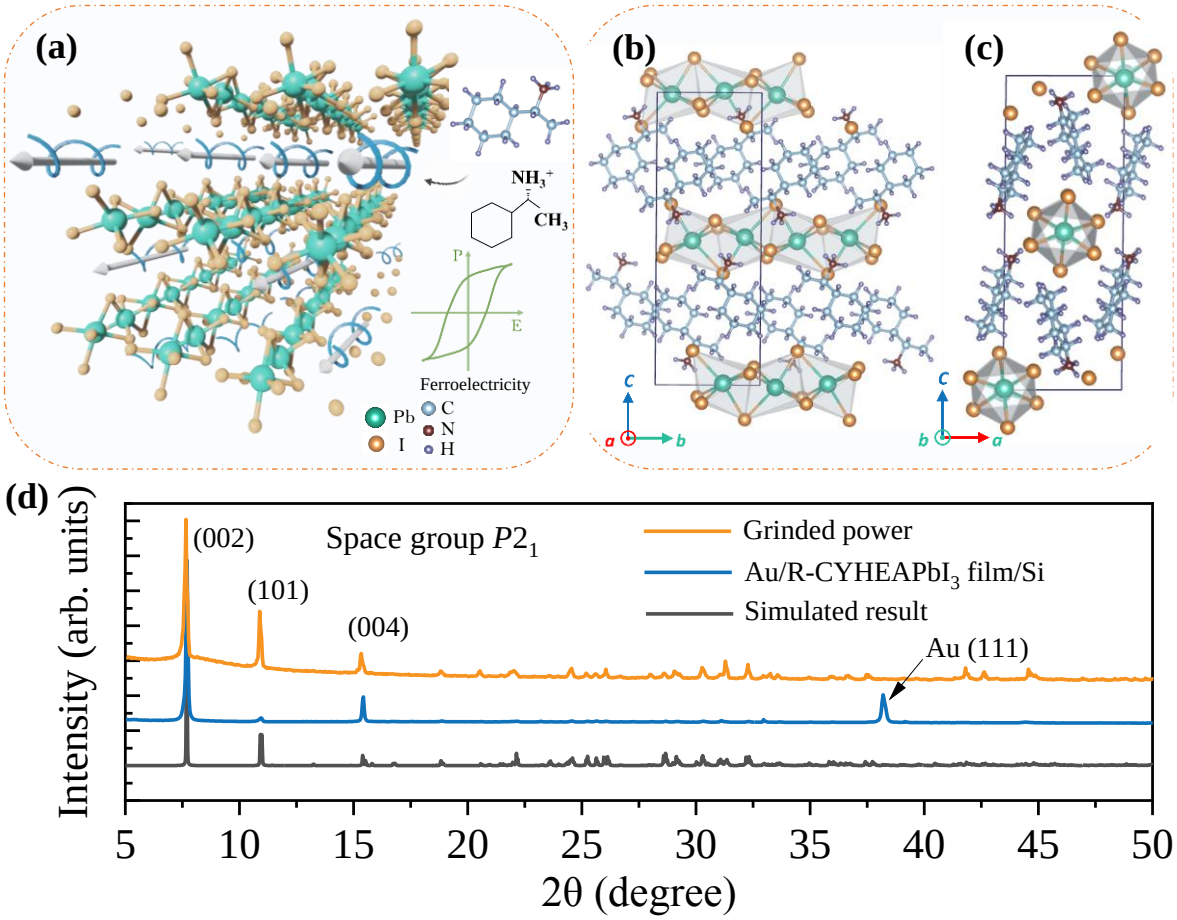

FIG. 1. *Ferroelectric 1D soft vdW halide perovskite R-CYHEAPbI$_3$. a) A schematic of R-CYHEAPbI$_3$ crystal structure consisting of lead halogen octahedra (PbI$_6$) and chiral organic groups. The helixes represent the chiral organic groups and the arrows represent the direction of ferroelectric polarization (b direction). Atomic structures of the R-CYHEAPbI$_3$ crystal: b) Side view from a direction and c) Side view from b direction. d) Experimental XRD results of grinded power form of R-CYHEAPbI$_3$, spin-coating film compared to the simulated one. The Au (111) peak rises from the top Au electrode.*

The ferroelectric property of R-CYHEAPbI$_3$ at both single crystal and thin film forms has been reported in our previous work.[26] More information about the intrinsic properties of R-CYHEAPbI$_3$ can be found in our previous work in ref[26]. It is shown that the polar axis of R-CYHEAPbI$_3$ is *b* direction. Similar as many other vdW materials,[30] when its thin film form is developed, most grains align their nonpolar axes (the axes that are perpendicular to the vdW gap planes) along the out-of-plane direction of the film and only a small portion of grains with their polar axes get aligned with the out-of-plane direction of the film.[26] Under a vertical device configuration, the ferroelectric polarization of the device is thus proportional to the percentage of the grains with *b* axis aligned along the out-of-plane direction of the film. Such relation has been experimentally confirmed in our previous work.[26] Based upon our current and former understanding of the ferroelectric property of R-CYHEAPbI$_3$ material, we further fabricate the synaptic device and explore the synaptic behaviors (Fig. 2(a)) based on thin film structure of R-CYHEAPbI$_3$. The schematic and morphology of the two-terminal ferroelectric diode is shown in Fig. S1(a) and S1(b) (in the Supplemental Material), in which R-CYHEAPbI$_3$ thin film is sandwiched between the top Au electrode and the bottom n-type Si (n-Si). The polarization-electric field measurement (Fig. S1(c)) shows that the magnitude of ferroelectric polarization of our thin film is consistent with previously reported ones. Figure S1(d) confirms the stable I-V curves with applied voltages from −0.6 V to 0.6 V for 50 loops.

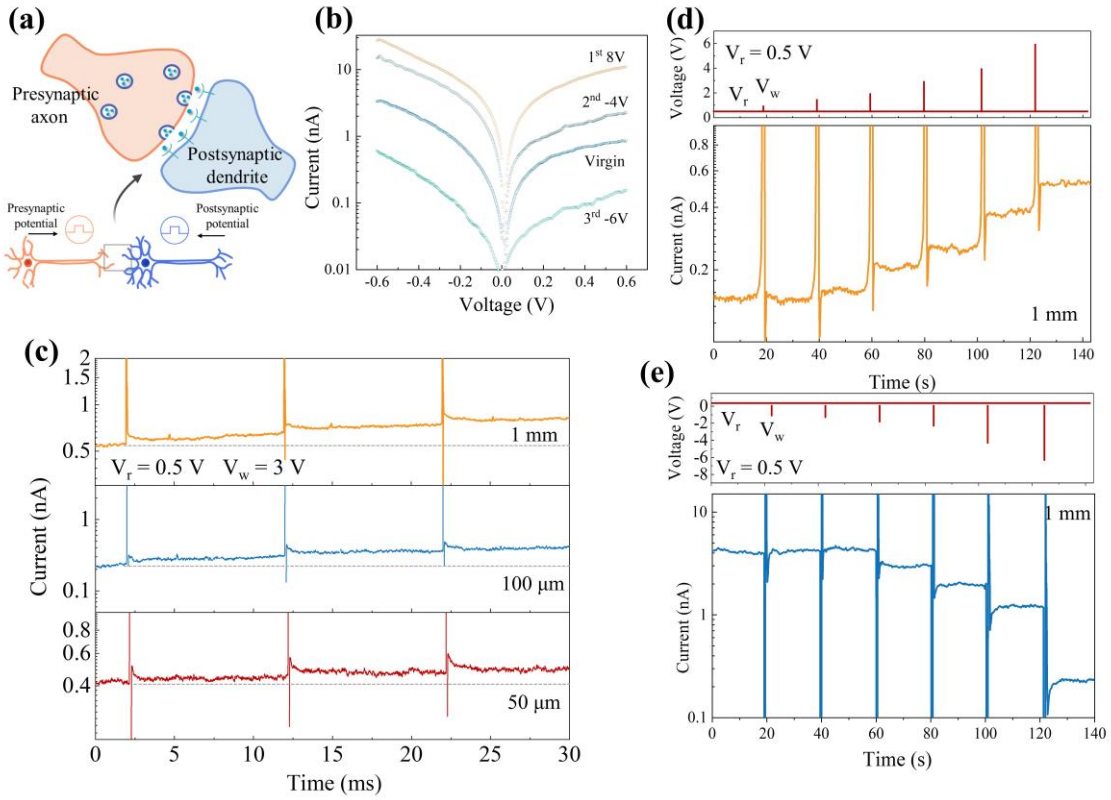

FIG. 2. *Characterizations of a two-terminal R-CYHEAPbI$_3$ ferroelectric diode. a) Our proposed ferroelectric synaptic device mimics the biological synapse whose weight is modified by presynaptic and postsynaptic potentials. b) I-V curves of R-CYHEAPbI$_3$ ferroelectric device at different poling voltages following a poling sequence of "virgin" →8 V for 30 s→−4 V for 30 s→−6 V for 30 s. c) Variable EPSCs of R-CYHEAPbI$_3$ ferroelectric device with the different Au electrode diameters of 1 mm, 100 µm and 50 µm, respectively. The write voltage (V_w) is 3 V with a duration of 500 µs, and the read voltage (V_r) is 0.5 V. d) and e) Varying resistances after positive and negative write voltage (V_w) with a pulse of 0.5 s. The read voltage (V_r) is 0.5 V and read length is almost 20 s.*

III. RESULTS AND DISCUSSION

The weight of R-CYHEAPbI$_3$ synapse is emulated by the resistance of ferroelectric diode which is a function of the relative fraction of aligned ferroelectric domains.[31] External write voltage pulses applied on the device are expected to modify the fraction of aligned domains, thus causing resistance to change.[32] Figure 2(b) shows I-V curves of our device Au/R-CYHEAPbI$_3$/Si with the Au electrode diameter of 1 mm after different write voltage (V_w) pulses (Au electrode is the positive terminal) with the duration of 30 s. For each V_w, the following sequence is virgin state (0 V) →first pulse (8 V) → second pulse (−4 V) → third pulse (−6 V). A large dynamic window of the forward current (at 0.5 V read voltage, V_r) of two orders of magnitude is observed. With the designed voltage poling sequence, we have observed that a positive voltage leads to a drop in resistance, while a negative voltage pulse gives a rise. Since our film is relatively thick beyond the tunneling regime, the transport behavior of our ferroelectric diode could be understood from thermionic model involving the potential barriers modified by ferroelectric polarization. The observation in Fig. 2(b) thus shows that voltage-tuned ferroelectric polarization can change the synaptic weight of our device. We adopted pulsed V_w on the R-CYHEAPbI$_3$ synapses with three different electrode diameters of 1 mm, 100 µm, 50 µm, respectively, to study the synaptic characteristics. As shown in Fig. 2(c), V_w of 3 V with the pulse duration of 500 µs as the presynaptic spikes applied on the Au electrode can bring the variable excitatory postsynaptic currents (EPSCs). The EPSCs of R-CYHEAPbI$_3$ synapses increase under a positive presynaptic spike (or V_w). Investigations of voltage pulse-dependent weight update at constant voltage duration per pulse are

conducted also with the results shown in Figs. 2(d) and 2(e) in which V_r is fixed to be 0.5 V and six different voltage pulses are employed, respectively. It is shown that positive or negative V_w pulses with increasing voltage magnitudes and a same pulse duration of 0.5 s lead to varying degrees of change in resistance. When the magnitude of positive or negative V_w are bigger than 2 V, the resistances of ferroelectric diode can have significant changes.

Figure 3(a) shows resistance-V_w hysteresis loops with resistance measured at V_r of 0.5 V. In characterizing the resistance-write voltage loop, V_w pulses are continuously applied following the path of 0 V → 9.2 V → (−6.4 V) → 0 V. It is found that R-CYHEAPbI$_3$ synapses can switch between high resistance state (HRS, R_{max} ~3×10^9 Ω) and low resistance state (LRS, R_{min} ~6×10^7 Ω) continuously. A higher V_w leads to a larger change of resistance, implied by the slope of resistance-write voltage curves. When V_w is above 8 V or below −5.6 V, resistance change pauses suggesting that the polarization may reach its saturation values. Overall, resistance change follows a multiple-state transition with a resistance span of almost 50 times.

Figures 3(b),3(c) illustrate the proposed resistance switching mechanism. The observed resistance switching can be explained by the tuning of height of potential barrier and the width of depletion region at the R-CYHEAPbI$_3$/electrode interface.[33-35] When current flows from Au to Si, the barrier height at R-CYHEAPbI$_3$/electrode interface determines its value.[32, 34-36] Specifically, after applying a positive V_w, some of ferroelectric dipoles point to n-Si (P_{down}). Positive bound charges at the R-CYHEAPbI$_3$/n-Si interface result in a reduced barrier height. [34, 35] In this case, under a small positive V_r, the device exhibits a relatively lower resistance than that before the positive write pulse is applied (Fig. 3(b)). In contrast, when some of the dipoles are flipped towards the Au electrode (P_{up}) under negative V_w, as shown in Fig. 3(c), the negative ferroelectric bound charges at R-CYHEAPbI$_3$/n-Si interface increases the barrier height. In this case, a higher resistance is expected.

As shown in Fig. 3(d), the LRS and HRS of synaptic devices are obtained after applying V_w of 10 V and −6.4 V with the duration of 30 s, respectively. The I-V characteristics of the device right after writing and after it is exposed in air for 24 hours are almost identical suggesting a good retention time of the analog states for our device. Figure 3(e) shows the retention performance of synaptic devices at HRS and LRS, in which no obvious deterioration is found within the 1000 s-duration reads. The R_{max}/R_{min} ratio of this synaptic device with R-CYHEAPbI$_3$ film at 100 nm in thickness is close to 50. Furthermore, we fabricated two-terminal R-CYHEAPbI$_3$ synapses with other two different thickness 160 nm (Fig. S2(a)) and 60 nm (Fig. S2(b)) with R_{max}/R_{min} ratio of 33 and 65, respectively. The dependence of R_{max}/R_{min} ratio on film thickness can be contributed the relative percentile of width of depletion region over the whole film thickness."[33-35] The polarization switching of R-CYHEAPbI$_3$ film was tested by using the PUND method (Experimental Section in Supplemental Material). After 10^7 bipolar switching cycles, the remanent polarization remains almost the same as the initial value of poled R-CYHEAPbI$_3$ film (Fig. 3(f), P_0 is the remanent polarization at first poling cycle).

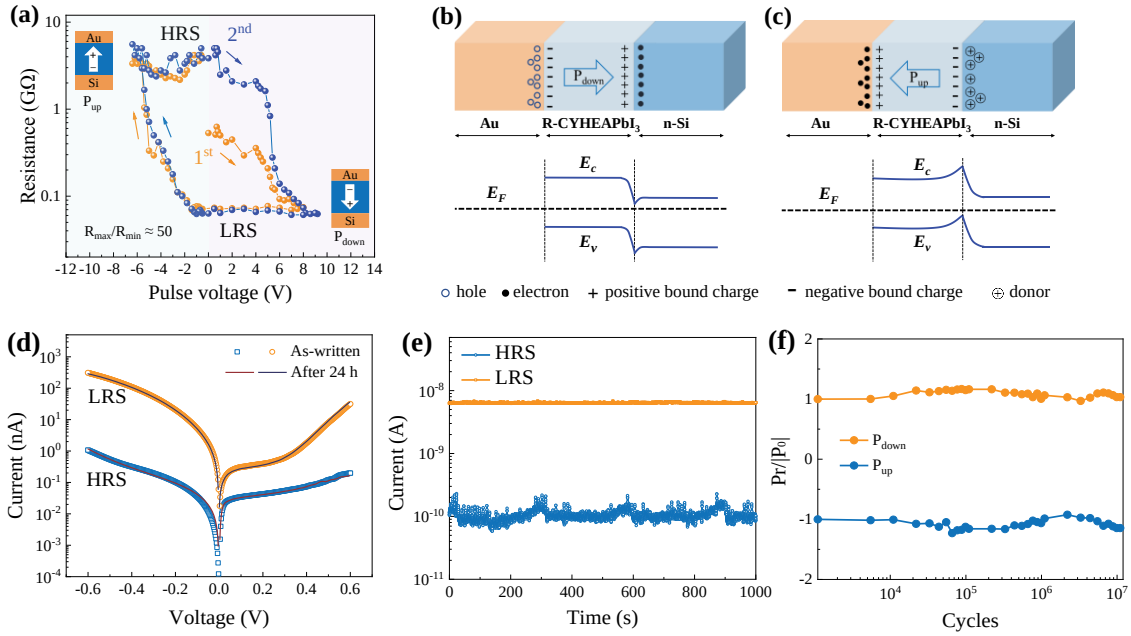

FIG. 3. *Tunable resistance of two-terminal R-CYHEAPbI$_3$ synapses. a) Resistance hysteresis loops versus pulse V_w (each pulse is 10 s). V_r is 0.5 V. Starting from the initial state of R-CYHEAPbI$_3$ device (the central orange point), two loops are collected. Schematics of polarization states are shown in the bottom-right (P_{down}) and top-left (P_{up}). Illustrations of ferroelectric polarization-modified carrier distributions and band diagrams: b) Ferroelectric polarization points to n-Si interface (P_{down}) after applying positive V_w; c) Ferroelectric polarization points to Au electrode (P_{up}) after applying negative V_w. E_F, E_c and E_v represents Fermi level, conduction band minimum and valence band maximum, respectively. d) Comparisons of I-V curves of as-written and after 24 h LRS and HRS. e) The retention performance of synaptic devices at HRS and LRS with 1000 s-duration reads. f) Fatigue endurance tests of remanent polarization.*

The STP and LTP are the basis synaptic functionalities executing neural computation.[37, 38] Typical STP behaviors of our Au/R-CYHEAPbI$_3$/Si synapses can be obtained by applying small V_w pulses. As shown in Figs. S3(a) and S3b, EPSCs are trigged by a small V_w of 1 V with the duration of 500 μs and the magnitude of EPSCs decays fastly to the initial states, which indicates only termporal enhanced connection exists between two adjacent neurons.[39] Figure 4(a) shows the characteristic of PPF which reflects the activity-dependent enhancement of EPSC evoked by the second pulse.[40] The inset in Fig. 4(a) is the PPF performance with the pulse interval of 180 μs. The plasticity of PPF is calculated as the increased proportion of second peak current compared with the first peak current. [37] Under the paired-pulse with a magnitude of 1.5 V and each duration of 500 μs, the plasticity of PPF is near to zero indicating the influence of first EPSC are effectively eliminated when the stimuli with the pulse intervals are larger than 280 μs. In neurobiology, STP can be converted to LTP by applying enhanced magnitude or duration of external stimulation.[11] Figures S3(c) and S3(d) show the increasing EPSCs under V_w of 4 V with the duration of 500 μs, suggesting the characteristic of long-term memory in R-CYHEAPbI$_3$ synapses. Using the stimulus signals shown in Fig. S(3), the calculated energy consumptions per spike of R-CYHEAPbI$_3$ synapses with the Au electrode diameter of 1 mm are 27 pJ and 70 pJ, respectively, when conducting STP and LTP processing.[2] As the Au electrode diameter decreases to 50 μm, the energy consumptions per spike are 0.25 pJ and 6.6 pJ for STP and LTP processing, respectively. The electrode area dependence of energy consumption per synpatic operation suggests that one may futher reduce the power consumption by reducing the electrode area.

STDP, as a form of Hebbian learning, is closely related with the information processing and synaptic characteristic.[2, 37, 38] The changes of synaptic weight and the performances of long-term potentiation or depression depends on Δt, which is defined as the relative time interval of the pre- and postsynaptic spikes. To emulate the STDP functionality of R-CYHEAPbI$_3$ synapses, the Au electrode as the presynaptic neurons is connected to a multiplexer and the Si electrode is grounded (Fig. S4(a)). The multiplexer is used to convert the time difference between pre- and postsynaptic spikes, and the detail

circuitry and logic of multiplexer can be found in Figs. S4b and S4c.[6, 41] As shown in Fig. S4(b), the adopted asymmetric STDP is conducted with the principle that the voltage pulse with the duration of 500 μs is proportional to Δt. Figure 4(b) shows the measured nonvolatile modifications of synaptic weight (the conductance of R-CYHEAPbI$_3$ synapses) with different initial resistance states. When a post-synaptic spike is fired before a pre-synaptic spike (Δt＜0), a negative voltage pulse is applied on the Au electrode leading to a synaptic depression, while the synaptic potentiation occurs if Δt＞0. Moreover, with a shorter Δt, a larger change of synaptic weight is obtained.

Figure 4(c), 4(d) show the demonstration of synaptic potentiation and depression of LTP using R-CYHEAPbI$_3$ synapses. We adopted different write schemes: scheme 1 includes a depressing voltage of −3.4 V and potentiating voltage of 5.8 V; scheme 2 includes a depressing voltage of −3.6 V and potentiating voltage of 6.2 V; other three write schemes (3, 4 and 5) can be seen in Fig. S(5). Each V_w pulse lasts for 0.5 s. Both write schemes 1 and 2 lead to 50 resistance states (V_r is 0.5 V). Following the definition of linearity of synaptic device,[14, 42] we find that using scheme 1, the linearity of depression $A_{d,1}$ is 0.4503 and potentiation $A_{p,1}$ is −0.4992. In scheme 2, the linearity of depression $A_{d,2}$ is 1.013 and potentiation $A_{p,2}$ is −0.6258. A larger absolute value of $A_{d,p}$ implies a better linearity for potentiation/depression (Experimental Section in Supplemental Material).[39, 42] Such linearity value is comparable to some of the best-performed artificial synapses (see Table S1). We also found that scheme 2 leads to a larger dynamic range which is reasonable as scheme 2 uses higher write voltages.[31]

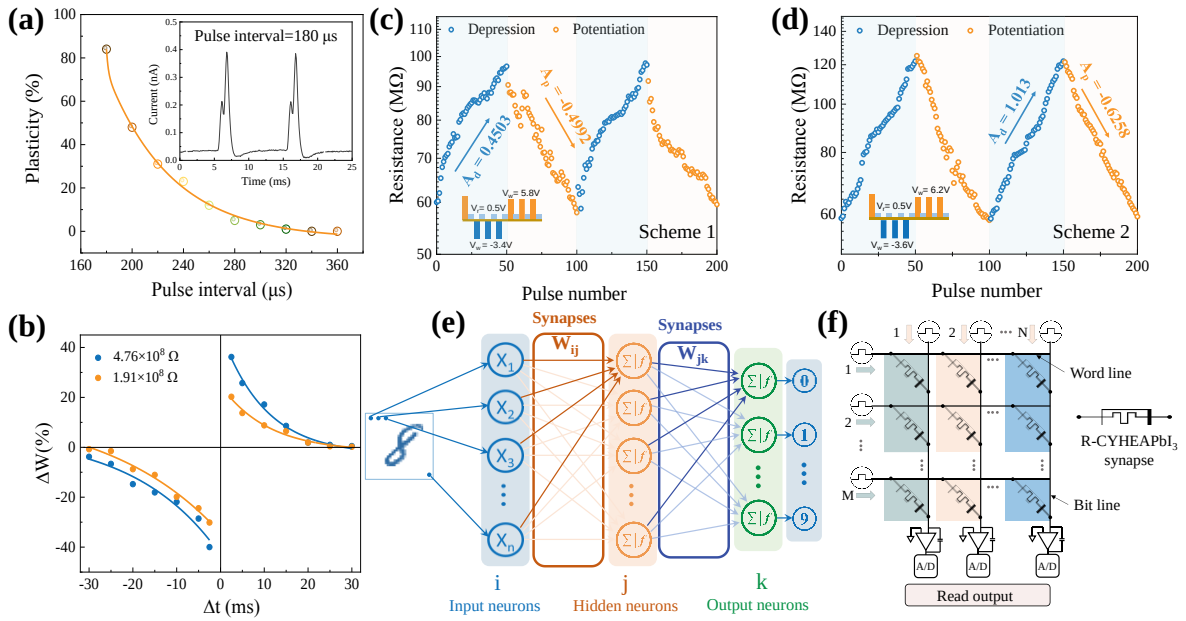

FIG. 4. *Write-read operations of R-CYHEAPbI$_3$ synapses and the neural network. a) PPF of R-CYHEAPbI$_3$ synapses under a paired-pulse with a magnitude of 1.5 V and each duration of 500 μs. The inset is the PPF performance with the pulse interval of 180 μs. b) STDP functionality of R-CYHEAPbI$_3$ synapses with the initial resistance of 4.76×10^8 Ω and 1.91×10^8 Ω. ΔW is the change ratio of conductance. Depressing and potentiating properties of R-CYHEAPbI$_3$ synapses with two different write schemes: c) Scheme 1 and d) Scheme 2. V_r and corresponding V_w with a pulse of 0.5 s are shown schematically in the bottom-left insets. The depressing and potentiating V_w are −3.4 V and 5.8 V for Scheme 1, −3.6 V and 6.2 V for Scheme 2, respectively. V_r is 0.5 V and both schemes start from the initial R_{min} state. $A_{d,p}$ represent the write linearity. e) Schematic of our proposed two-layer neural network. $\mathbf{W}_{ij}$ and $\mathbf{W}_{jk}$ represent the weight matrices. f is sigmoid nonlinear activation function. f) Our proposed crossbar structure with M input rows (word lines) and N output columns (bit lines) based on R-CYHEAPbI$_3$ synapses for performing the analog matrix operations.*

To evaluate the potential of R-CYHEAPbI$_3$ synapse in neural network for learning tasks like pattern recognition, as shown in Figs. 4(e) and 4(f), we designed R-CYHEAPbI$_3$ synapses into a two-layer neural network (one hidden layer) based on two crossbar arrays. In Fig. 4(e), $\mathbf{W}_{ij}$ and $\mathbf{W}_{jk}$ represent the

weight matrices connecting the input layer to the hidden layer (the first crossbar array) and the hidden layer to the output layer (the second crossbar array), respectively. As illustrated in Fig. 4(f), the crossbar array with M input rows (word lines) and N output columns (bit lines) was used to carry out the parallel read and write operations. Individual synapse ij and jk can be reached from i^{th} word line/j^{th} bit line and j^{th} word line/k^{th} bit line, respectively.[43] With this, we conducted supervised learning with back propagation algorithm and sigmoid nonlinear activation function (details in Fig. S(6)).[43-45] This artificial neural network was trained with two data sets: an 8 × 8 pixel image version of handwritten digits[46] and a 28 × 28 pixel image version of handwritten digits.[47] The training and classification information associated with 8 × 8 and 28 × 28 image sets is summarized in Table S2. Learning rate η = 0.1 was used for training both two image sets.

Figure 5(a)-5(f) show the weight patterns and distributions of synapses connecting the input layer to the hidden layer at different training epochs (for 8 × 8 imagine set). [48, 49] The corresponding matrix is 64 (input elements) × 36 (output elements). The weight patterns and distributions evolution for 28 × 28 image set are presented in Figs. S(7) and S(8). The initial weights (0^{th} epoch) of R-CYHEAPbI$_3$ synapses are generated randomly (Fig. 5(a) and Fig. S7(a)). To minimize the negative impact of synaptic nonlinearity and write/read noise, and to prevent potential weight saturation, weights of R-CYHEAPbI$_3$ synapses are set to stay in 25% to 75% of the whole conductance range during training.[43] It can be seen that after training weight distributions profile exhibit multiple peaks spanning in a relatively reasonable range shown in Figs. 5(e), 5(f) and Fig. S(8). From the probability density of synaptic conductance (Figs. 5(d)-5(f) and Fig. S(8)), we can see that weights are updated rapidly after the first few training epochs and then remain relatively stable. This indicates that a highly efficient training is achieved within a few iterations.

Figure 5(g) shows that reasonable classification accuracies can be reached very rapidly during training. For example, for 8 × 8 image set, after five epochs, for training scheme 1, the classification accuracy reaches 85.1%. For training scheme 2, it is 91.5%. The better performance of scheme 2 is likely due to its better synaptic linearity.[1] Figure 5(h) shows similar observation in which the training data set is 28 × 28 image set. Compared to the classification accuracy of ideal numeric that is from the floating-point-based neural network performance,[1, 37] the classification accuracies of both scheme 1 and 2 are slightly lower for 8 × 8 image set. [43] Figure S9(a) shows the classification accuracies of 8 × 8 image set obtained using 0 to 100% and 25% to 75% of the scheme 1 and 2 weight range. It can be seen that the classification accuracies using 25% to 75% of the weight range indeed can reach a higher value. The comparisons of classification accuracies using scheme 1 to 2 can also prove that a better linearity is helpful for achieving good computing results. A comparison of the performance of our R-CYHEAPbI$_3$ synapse with several typical memristive devices is shown in Table S1. [37, 39, 50-55] From Table S1, it can be seen that the energy consumption per synaptic operation for our vdW system is comparable or better than several synaptic systems, making it as a promising candidate for brain-like computing. Although the dynamic range of weights in our synapses is smaller than some of former devices, [14, 37, 50, 52] R-CYHEAPbI$_3$ device still exhibits a good linearity and small cycle-to-cycle variation, which seem to contribute more on receiving better accuracies.

IV. CONCLUSION

In summary, we propose and experimentally demonstrate a vdW halide perovskite-based ferroelectric synapse. We show that individual devices exhibit a promising synaptic linearity and low cycle-to-cycle variation. By optimizing the voltage pulse parameters, the R-CYHEAPbI$_3$ synapses can process with a switching speed within hundreds of microseconds and an energy consumption per spike at pico joule level for the STP and LTP operations. Crossbar-structured two-layer neural network simulations based on R-CYHEAPbI$_3$ synapses with back propagation algorisms show that our synaptic device and circuit can perform efficient learning and reach reasonable classification accuracy (92%) with a low number of training epochs. Our work suggests the prospective potential of ferroelectric vdW halide perovskite in energy-efficient information processing and computing.

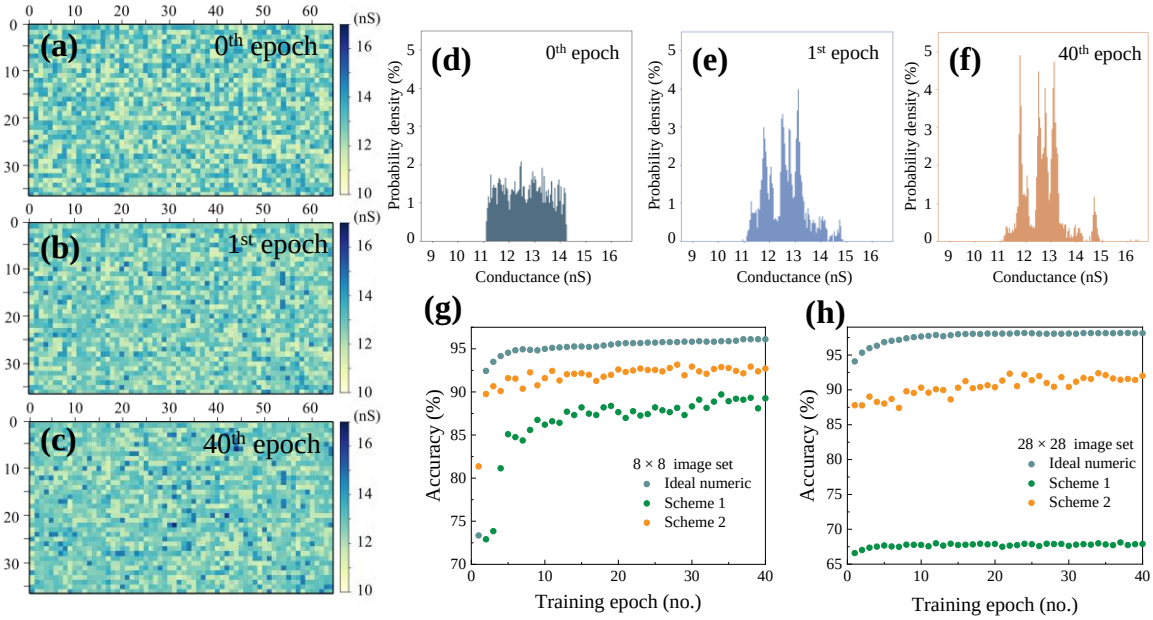

FIG. 5. *Pattern recognition using proposed neural network following back propagation algorithm. a-f) Weight (conductance) distributions and the corresponding probability density plots of the first crossbar array (connecting the input layer to the hidden layer) during training with synaptic plasticity following the one in Fig. 4(b) (scheme 2): (a) and (d) initial state (the 0th epoch); (b) and (e) after the 1st training epoch; (c) and (f) after the 40th training epoch. Each pixel in (a)-(c) represents the conductance of each R-CYHEAPbI$_3$ synapse in the first crossbar array. g) and h) Classification accuracies versus training epochs for 8 × 8 and 28 × 28 image sets, respectively.*

Supplemental Material Experimental Section, additional information and figures, including polarization-electric loop and transport characteristics, STP and LTP behaviors, the realization of STDP, depressing and potentiating properties of R-CYHEAPbI$_3$ ferroelectric diode; details of pattern classification simulation.

Data and code availability

Data and code are available from the corresponding authors upon reasonable request.

Conflict of interest

The authors declare no competing financial interest.

Acknowledgements

Y.C. and C.S. acknowledge the support from China Scholarship Council, National Natural Science Foundation of China (Grant No. 61974107). J.S. and L.Z. acknowledge the support from National Science Foundation under award No. 1916652 and NYSTAR under contract C180117. The authors would like to acknowledge Prof. Sapan Agarwal (Research Scientist at Sandia National Laboratories), Prof. Rongjie. Lai and Ms. Jiajia Yu (Department of Mathematics, Rensselaer Polytechnic Institute) for the discussions about neuromorphic algorithm and Prof. Qidong Tai and Dr. Xiang Zhang (Wuhan University) for the material growth.

*Corresponding authors: Chengliang Sun (sunc@whu.edu.cn) and Jian Shi (shij4@rpi.edu)

References

[1] E. J. Fuller, S. T. Keene, A. Melianas, Z. Wang, S. Agarwal, Y. Li, Y. Tuchman, C. D. James, M. J. Marinella, J. J. Yang, Parallel programming of an ionic floating-gate memory array for scalable neuromorphic computing, Science **364,** 570 (2019).

[2] C. Ge, G. Li, Q. L. Zhou, J. Y. Du, E. J. Guo, M. He, C. Wang, G. Z. Yang, K. J. Jin, Gating-induced reversible H_xVO_2 phase transformations for neuromorphic computing, Nano Energy **67**,104268 (2020).

[3] I. Boybat, M. Le Gallo, S. Nandakumar, T. Moraitis, T. Parnell, T. Tuma, B. Rajendran, Y. Leblebici, A. Sebastian, E. Eleftheriou, Neuromorphic computing with multi-memristive synapses, Nat. Commun. **9**, 1 (2018).

[4] S. D. Ha, J. Shi, Y. Meroz, L. Mahadevan, S. Ramanathan, Neuromimetic circuits with synaptic devices based on strongly correlated electron systems, Phys. Rev. Appl. **2**, 064003 (2014).

[5] J. Shi, Y. Zhou, S. Ramanathan, Colossal resistance switching and band gap modulation in a perovskite nickelate by electron doping, Nat. Commun. **5**, 1 (2014).

[6] J. Shi, S. D. Ha, Y. Zhou, F. Schoofs, S. Ramanathan, A correlated nickelate synaptic transistor, Nat. Commun. **4**, 1 (2013).

[7] M. J. Marinella, S. Agarwal, A. Hsia, I. Richter, R. Jacobs-Gedrim, J. Niroula, S. J. Plimpton, E. Ipek, C. D. James, Multiscale co-design analysis of energy, latency, area, and accuracy of a ReRAM analog neural training accelerator, IEEE J. Em. Sel. Top. C. **8**, 86 (2018).

[8] J. T. Yang, C. Ge, J. Y. Du, H. Y. Huang, M. He, C. Wang, H. B. Lu, G. Z. Yang, K. J. Jin, Artificial Synapses Emulated by an Electrolyte‐Gated Tungsten‐Oxide Transistor, Adv. Mater. **30**, 1801548 (2018).

[9] D. B. Strukov, G. S. Snider, D. R. Stewart, R. S. Williams, The missing memristor found, Nature **453**, 80 (2008).

[10] G. W. Burr, R. M. Shelby, S. Sidler, C. Di Nolfo, J. Jang, I. Boybat, R. S. Shenoy, P. Narayanan, K. Virwani, E. U. Giacometti, Experimental demonstration and tolerancing of a large-scale neural network (165000 synapses) using phase-change memory as the synaptic weight element, IEEE T. Electron Dev. **62**, 3498 (2015).

[11] J. Zhu, T. Zhang, Y. Yang, R. Huang, A comprehensive review on emerging artificial neuromorphic devices, Appl. Phys. Rev. **7**, 011312 (2020).

[12] S. Oh, H. Hwang, I. Yoo, Ferroelectric materials for neuromorphic computing, Apl. Mater. **7**, 091109 (2019).

[13] Z. Wen, D. Wu, Ferroelectric Tunnel Junctions: Modulations on the Potential Barrier, Adv. Mater. **32**, 1904123 (2019).

[14] M. Jerry, P.-Y. Chen, J. Zhang, P. Sharma, K. Ni, S. Yu, S. Datta, Ferroelectric FET analog synapse for acceleration of deep neural network training, 2017 IEEE International Electron Devices Meeting (IEDM), IEEE, **6**, 2 (2017).

[15] Y. Chen, Y. Zhou, F. Zhuge, B. Tian, M. Yan, Y. Li, Y. He, X.S. Miao, Graphene–ferroelectric transistors as complementary synapses for supervised learning in spiking neural network, npj 2D Mater. Appl. **3**,1 (2019).

[16] H. Li, R. Wang, S. Han, Y. Zhou, Ferroelectric polymers for non‐volatile memory devices: a review, Polym. Int. **69**, 533 (2020).

[17] I. Raifuku, Y. P. Chao, H. H. Chen, C. F. Lin, P. E. Lin, L. C. Shih, K. T. Chen, J. Y. Chen, J. S. Chen, P. Chen, Halide perovskite for low‐power consumption neuromorphic devices, EcoMat **3**, e12142 (2021).

[18] N. Pandech, T. Kongnok, N. Palakawong, S. Limpijumnong, W. R. Lambrecht, S. Jungthawan, Effects of the van der Waals Interactions on Structural and Electronic Properties of $CH_3NH_3(Pb,Sn)(I,Br,Cl)_3$ Halide Perovskites, ACS omega **5**, 25723 (2020).

[19] Y. Guo, W.A. Saidi, Q. Wang, 2D halide perovskite-based van der Waals heterostructures: contact evaluation and performance modulation, 2D Mater. **4**, 035009 (2017).

[20] J. Gong, H. Yu, X. Zhou, H. Wei, M. Ma, H. Han, S. Zhang, Y. Ni, Y. Li, W. Xu, Lateral artificial synapses on hybrid perovskite platelets with modulated neuroplasticity, Adv. Funct. Mater. **30**, 2005413 (2020).

[21] J. Gong, H. Wei, Y. Ni, S. Zhang, Y. Du, W. Xu, Methylammonium halide-doped perovskite artificial synapse for light-assisted environmental perception and learning, Mater. Today Phys. **21**, 100540 (2021).

[22] S. Chen, J. Huang, Recent Advances in Synaptic Devices Based on Halide Perovskite, ACS Appl. Electron Ma. **2**, 1815 (2020).
[23] G. Roma, A. Marronnier, J. Even, From latent ferroelectricity to hyperferroelectricity in alkali lead halide perovskites, Phys. Rev. Mater. **4**, 092402 (2020).
[24] H. Yu, J. Gong, H. Wei, W. Huang, W. Xu, Mixed-halide perovskite for ultrasensitive two-terminal artificial synaptic devices, Mater. Chem. Front. **3**, 941 (2019).
[25] J. Gong, H. Yu, H. Wei, Y. Zheng, C. Yuan, M. Ma, H. Han, K. Guo, J. Xu, W. Xu, An air-stable two-dimensional perovskite artificial synapse, Semicond Sci. Tech. **35**, 104001 (2020).
[26] Y. Hu, F. Florio, Z. Chen, W.A. Phelan, M.A. Siegler, Z. Zhou, Y. Guo, R. Hawks, J. Jiang, J. Feng, A chiral switchable photovoltaic ferroelectric 1D perovskite, Sci. Adv. **6**, eaay4213 (2020).
[27] K. Momma, F. Izumi, VESTA 3 for three-dimensional visualization of crystal, volumetric and morphology data, J. Appl. Crystallogr. **44**, 1272 (2011).
[28] L. You, Y. Zhang, S. Zhou, A. Chaturvedi, S. A. Morris, F. Liu, L. Chang, D. Ichinose, H. Funakubo, W. Hu, Origin of giant negative piezoelectricity in a layered van der Waals ferroelectric, Sci. Adv. **5**, eaav3780 (2019).
[29] See the Supplemental Material at URL which includes Refs. [14, 26, 27, 37, 39, 42, 46-55], for details of Experimental Section, write linearity of R-CYHEAPbI$_3$ synapses.
[30] J. Choi, J. S. Han, K. Hong, S. Y. Kim, H. W. Jang, Organic–inorganic hybrid halide perovskites for memories, transistors, and artificial synapses, Adv. Mater. **30**, 1704002 (2018).
[31] A. Chanthbouala, V. Garcia, R. O. Cherifi, K. Bouzehouane, S. Fusil, X. Moya, S. Xavier, H. Yamada, C. Deranlot, N. D. Mathur, A ferroelectric memristor, Nat. Mater. **11**, 860 (2012).
[32] S. Boyn, J. Grollier, G. Lecerf, B. Xu, N. Locatelli, S. Fusil, S. Girod, C. Carrétéro, K. Garcia, S. Xavier, Learning through ferroelectric domain dynamics in solid-state synapses, Nat. Commun. **8**, 1 (2017).
[33] R. Meyer, R. Waser, Hysteretic resistance concepts in ferroelectric thin films, J. Appl. Phys. **100**, 051611 (2006).
[34] Z. Hu, Q. Li, M. Li, Q. Wang, Y. Zhu, X. Liu, X. Zhao, Y. Liu, S. Dong, Ferroelectric memristor based on Pt/BiFeO3/Nb-doped SrTiO3 heterostructure, Appl. Phys. Lett. **102**, 102901 (2013).
[35] Z. Wen, C. Li, D. Wu, A. Li, N. Ming, Ferroelectric-field-effect-enhanced electroresistance in metal/ferroelectric/semiconductor tunnel junctions, Nat. Mater. **12**, 617 (2013).
[36] M. Lallart, Ferroelectrics: Physical Effects, BoD–Books on Demand, (2011).
[37] J. Li, C. Ge, J. Du, C. Wang, G. Yang, K. Jin, Reproducible Ultrathin Ferroelectric Domain Switching for High‐Performance Neuromorphic Computing, Adv. Mater. **32**, 1905764 (2020).
[38] G. Q. Bi, M. M. Poo, Synaptic modification by correlated activity: Hebb's postulate revisited, Annu. Rev. Neurosci. **24**, 139 (2001).
[39] M. K. Kim, J. S. Lee, Ferroelectric analog synaptic transistors, Nano Lett. **19**, 2044 (2019).
[40] J. X. Bao, E. R. Kandel, R. D. Hawkins, Involvement of pre-and postsynaptic mechanisms in posttetanic potentiation at Aplysia synapses, Science. **275**, 969 (1997).
[41] Y. Nishitani, Y. Kaneko, M. Ueda, T. Morie, E. Fujii, Three-terminal ferroelectric synapse device with concurrent learning function for artificial neural networks, J. Appl. Phys. **111**, 124108 (2012).
[42] P. Y. Chen, X. Peng, S. Yu, NeuroSim: A circuit-level macro model for benchmarking neuro-inspired architectures in online learning, IEEE T. Comput. Aid. D. **37**, 3067 (2018).
[43] S. Agarwal, S. J. Plimpton, D. R. Hughart, A. H. Hsia, I. Richter, J. A. Cox, C. D. James, M. J. Marinella, Resistive memory device requirements for a neural algorithm accelerator, 2016 International Joint Conference on Neural Networks (IJCNN), IEEE, 929 (2016).
[44] E. J. Fuller, F. E. Gabaly, F. Léonard, S. Agarwal, S. J. Plimpton, R. B. Jacobs‐Gedrim, C. D. James, M. J. Marinella, A. A. Talin, Li-ion synaptic transistor for low power analog computing, Adv. Mater. **29**, 1604310 (2017).
[45] Y. van de Burgt, E. Lubberman, E. J. Fuller, S. T. Keene, G. C. Faria, S. Agarwal, M. J. Marinella, A. A. Talin, A. Salleo, A non-volatile organic electrochemical device as a low-voltage artificial synapse for neuromorphic computing, Nat. Mater. **16**, 414 (2017).
[46] K. Bache, M. Lichman, University of California at Irvine, School of Information and Computer Science, Irvine, CA, USA, 2013.
[47] Y. LeCun, L. Bottou, Y. Bengio, Haffner, Gradient-based learning applied to document recognition. P. Proc. IEEE, **86**, 2278 (1998).
[48] J. Crodelle, D.W. McLaughlin, Idealized model of the developing visual cortex, bioRxiv (2020).

[49] P. Voosen, How AI detectives are craking open the black box of deep learning, Science (2017).
[50] J. Woo, K. Moon, J. Song, S. Lee, M. Kwak, J. Park, H. Hwang, Improved synaptic behavior under identical pulses using AlO*x*/HfO_2 bilayer RRAM array for neuromorphic systems, IEEE Electr. Device L. **37**, 994 (2016).
[51] H. Mulaosmanovic, E. T. Breyer, T. Mikolajick, S. Slesazeck, Recovery of cycling endurance failure in ferroelectric FETs by self-heating, IEEE Electr. Device L. **40**, 216 (2018).
[52] S. H. Jo, T. Chang, I. Ebong, B. B. Bhadviya, P. Mazumder, W. Lu, Nanoscale memristor device as synapse in neuromorphic systems, Nano Lett. **10**, 1297 (2010).
[53] S. Oh, T. Kim, M. Kwak, J. Song, J. Woo, S. Jeon, I. K. Yoo, H. Hwang, HfZrO*x*-based ferroelectric synapse device with 32 levels of conductance states for neuromorphic applications, IEEE Electr. Device L. **38**, 732 (2017).
[54] Y. Li, E.J. Fuller, S. Asapu, S. Agarwal, T. Kurita, J. J. Yang, A. A. Talin, Low-voltage, CMOS-free synaptic memory based on Li*x*TiO_2 redox transistors, ACS Appl. Mater. Inter. **11**, 38982 (2019).
[55] S. Choi, J. Yang, G. Wang, Emerging Memristive Artificial Synapses and Neurons for Energy‐Efficient Neuromorphic Computing, Adv. Mater. **32**, 2004659 (2020).